Research Article | Vol. 12, No. 6 / 1 June 2021 / Biomedical Optics Express 3619
Biomedical Optics EXPRESS

High resolution optical projection tomography platform for multispectral imaging of the mouse gut

CÉDRIC SCHMIDT,[1,*] ARIELLE L. PLANCHETTE,[2] DAVID NGUYEN,[3] GABRIEL GIARDINA,[1] YOAN NEUENSCHWANDER,[1] MATHIEU DI FRANCO,[1] ALESSIO MYLONAS,[2] ADRIEN C. DESCLOUX,[2] ENRICO POMARICO,[1] ALEKSANDRA RADENOVIC,[2] AND JÉRÔME EXTERMANN[1]

[1]*HEPIA/HES-SO, University of Applied Sciences of Western Switzerland, Rue de la Prairie 4, 1202 Geneva, Switzerland*
[2]*Laboratoire de Biologie à l'Échelle Nanométrique, School of Engineering, École Polytechnique Fédérale de Lausanne, CH-1015 Lausanne, Switzerland*
[3]*Zlatic Lab, Neurobiology, MRC-Laboratory of Molecular Biology, Cambridge CB2 0QH, United Kingdom*
[*]*cedric.schmidt@hesge.ch*

Abstract: Optical projection tomography (OPT) is a powerful tool for three-dimensional imaging of mesoscopic biological samples with great use for biomedical phenotyping studies. We present a fluorescent OPT platform that enables direct visualization of biological specimens and processes at a centimeter scale with high spatial resolution, as well as fast data throughput and reconstruction. We demonstrate nearly isotropic sub-28 µm resolution over more than 60 mm^3 after reconstruction of a single acquisition. Our setup is optimized for imaging the mouse gut at multiple wavelengths. Thanks to a new sample preparation protocol specifically developed for gut specimens, we can observe the spatial arrangement of the intestinal villi and the vasculature network of a 3-cm long healthy mouse gut. Besides the blood vessel network surrounding the gastrointestinal tract, we observe traces of vasculature at the villi ends close to the lumen. The combination of rapid acquisition and a large field of view with high spatial resolution in 3D mesoscopic imaging holds an invaluable potential for gastrointestinal pathology research.

1. Introduction

Mesoscopic imaging focuses on samples typically ranging from a few millimeters up to several centimeters in at least one dimension [1]. This range is generally not accessible to optical microscopy techniques such as confocal and multiphoton microscopy which use raster scanning to produce volumetric images, thus limiting the sample size to less than 1 mm for a reasonable acquisition time [1]. At the mesoscopic scale imaging whole animal organ portions becomes possible, thus providing the opportunity to investigate their global structural organization, as well as biological functionalities. In particular, systematic longitudinal imaging of intact gut tissues is a desirable tool to advance our understanding of the fundamental interactions between the enteric nervous system, the immune system, the epithelial barrier and microbes. Such imaging range can also be exploited for the molecular diagnosis of Parkinson's disease. Recent studies using conventional microscopy have revealed the presence of Lewy Bodies in the intestine, and highlighted their usefulness as early reliable biomarkers of the disease [2–4]. However, this method is challenging to apply in routine diagnostics because of poor tissue sampling in standard histological methods occurring when dealing with elongated specimens. The added advantages of using whole-tissue imaging are reliable and global biological marker characterization and quantification, therefore decreasing the need for repeated endoscopic interventions.

#423284 https://doi.org/10.1364/BOE.423284
Journal © 2021 Received 26 Feb 2021; revised 6 May 2021; accepted 18 May 2021; published 26 May 2021

Biomedical Optics EXPRESS

While mesoscopic imaging is mainly conveyed by light sheet fluorescence microscopy (LSFM) [5], optical projection tomography (OPT) [6] differs in that it comes with reduced complexity, lower cost, and an alternative scanning geometry. In LSFM, the illumination consists of a well-defined sheet of light generated by a laser and that is orthogonal to the detection path. Recently, LSMF has been used in a humanized mouse model to image Human T cells in the ileocolic artery of colitic immunodeficient mice and demonstrated the translational value of the 3D imaging of the inflamed murine gut [7]. On the other hand, OPT can be understood as the optical equivalent of the x-ray computed tomography (CT) [8,9] or the micro-CT [10] for smaller specimens: a camera acquires a sequence of bright-field or fluorescence images (or projections) of the sample upon rotation at equally spaced angular orientations. The sample is then reconstructed using a suitable algorithm [11]. Both LSFM and fluorescent OPT allow spectral decomposition of the measured signal. This feature provides enhanced tissue specificity as compared to higher-energy scanning techniques such as x-ray imaging, where tissue identification is performed via light attenuation measurements. Although LSFM can provide a higher lateral resolution with respect to OPT (typically sub-μm in at least one dimension), its intrinsic anisotropy between axial and lateral resolution could induce ambiguity in 3D analysis [12]. For this reason, and because of its rotational scanning geometry, we consider OPT to be competitive for imaging long samples with cylindrical symmetry, such as the mouse gut.

Since its first demonstration, the OPT scheme has been adopted for a variety of applications, including imaging of zebrafish embryos [13,14] and their cardiovascular system [15,16], mouse organs [17–19], as well as plants [20], in both transmission and epi-detection geometries. In preclinical research, pancreas imaging via OPT [17,21] has been shown to play a key role in diabetes research, providing scientists with a quantitative overview of the disease progression in the entire mouse organ. Similarly, whole mouse brain imaging was performed with OPT for the study of Alzheimer's disease [22,23]. Technical advances have come with the growth of OPT applications in preclinical research. For instance, helical scanning has been proposed to increase the field of view (FOV) [24], fluorescence lifetime measurements has demonstrated enhanced tissue specificity [14,25], coherent LASER illumination has enabled measurement of blood flow [26,27] and tomography acquisition has been combined with LSFM in hybrid instruments for artefact correction [28–30]. At the same time, advanced reconstruction algorithms based on light field retrieval [31–34], resolution improvement using point-spread-function (PSF) deconvolution [35–37], tissue absorption measurements [38] and iterative reconstruction allowing reduced acquisition time [24,39,40], have been developed.

Here, we present the first multispectral fluorescent OPT platform suited to mouse gut imaging. To this end, we introduce a new sample preparation technique, based on a virtually cut-free specimen embedding procedure via molding in cylindrical tubes. This method allows one to uniformize sample shape, as well as reduce sample damage and imaging artefacts as compared to standard sample preparation [41,42]. In addition, we design our setup to optimize the trade-off between the sample size and the lateral resolution induced by visible light diffraction limitations [43]. We provide accurate measurements of the resolving power of the instrument based on the reconstructed PSF of 1 μm diameter fluorescent microspheres and demonstrate a sub-28 μm resolution along the 3 dimensions. Finally, we present a reconstructed 3-cm long gut portion with two spectral channels to emphasize the vascular system network surrounding the intestinal villi structure.

Biomedical Optics EXPRESS

2. Methods

2.1. Sample preparation protocol

2.1.1. Trans-cardiac perfusion and fixation

Mice were generated and housed at the École Polytechnique Fédérale de Lausanne and handled in accordance with the guidelines and regulations of the institution and of the state of Vaud (authorization number VD3448). Animals are deeply anesthetized by intra-peritoneal injection of 50 mg/kg of sodium pentobarbital. Upon disappearance of reflexes, the mice are perfused with 10 ml of heparinized PBS (5 I.U./ml Liquemin) followed by 10 ml of 4% paraformaldehyde (CAS 30525-89-4, Carl Roth AG 0964.1). Once samples of interest are collected, they undergo post-fixation overnight at 4°C.

2.1.2. Tissue fluorescence quenching and permeabilization

Samples are washed in PBS at room temperature for 30 minutes to remove excess paraformaldehyde. Tissue fluorescence quenching is performed by incubating the samples in a solution of MetOH:DMSO:H_2O_2 (as a 2:1:3 ratio) overnight. This is followed by tissue permeabilization, which is carried out by cycling through three freeze-thaw cycles (1hr at −80°C and 30 minutes at room temperature).

2.1.3. Antibody staining

The principle of staining whole organ samples is based on immuno-histochemical staining on a large scale. The samples are blocked in a buffer for 24 hours at room temperature followed by a 48-hour primary antibody incubation and a 24-hour wash in 0.1% TBS-Triton X-100 (UN3082, Applichem). Then, the samples undergo a 48-hour secondary antibody incubation and another 24-hour wash. Organ vasculature is stained by post-excision infusion staining of a rat anti-CD31 primary antibody targeting the murine platelet-endothelial cell adhesion molecule (Abcam ab7388). The secondary antibody is a goat anti-rat AlexaFluor 647 (Thermofisher A21247).

2.1.4. Mounting and clearing

The samples are mounted in 1.5% agarose using cylindrical open-ended molds made from 10 ml serological pipettes cut to optimal length. In order to center and straighten the intestinal tissue, the samples are pierced with strings on either end, which are used to adjust the sample's position within the cylinder. One end of the mold is closed using parafilm, to be filled with 1.5% agarose and allowed to set at room temperature. The agarose-enclosed samples are dehydrated for 24-hour in pure methanol (CAS 67-56-1, Sigma-Aldrich 322415), with two solution changes. Then, they are cleared using a 1:2 ratio of benzyl alcohol (CAS 100-51-6, Sigma-Aldrich 305197) and benzyl benzoate (CAS 120-51-4, Sigma-Aldrich B6630) (BABB). Clearing takes at least 72 hours prior to OPT acquisition. All the steps above are performed in the dark to prevent photo bleaching.

2.1.5. Fluorescent microsphere

For calibration and resolution analysis, we used 1 µm fluorescent FITC-labeled microspheres based on melamine resin (90305-5ML-F, Sigma). The sample preparation follows the previous steps with the beads as specimen. Approximately 0.01 ml of particle solution is mixed to 10 ml of 1.5% agarose before molding to achieve a nearly colloidal solution. The acquisition is performed shortly after the clearing process to avoid undesired fluorescence quenching of the signal induced by chemical reaction with either the methanol or the BABB.

Biomedical Optics EXPRESS

2.2. Acquisition setup

The optical design of our platform has been realized with commercially available optics. The imaging depth of field (DOF), FOV and optical resolution have been optimized for imaging a mouse gut with a diameter up to 5 mm over the whole visible range using OpticStudio 21.1 (Zemax LLC). In order to reduce the number of sections during sample preparation, the positioning mechanism allows specimens up to 10 cm in length to be acquired. A schematic of the setup is shown in Fig. 1. Sample illumination is provided by several LEDs on metal-core PCBs (MxxxD2,3 series, Thorlabs) of different central wavelengths, mounted on heat dissipators and filtered out using bandpass filters. An aspheric condenser lens (ACL25416U, Thorlabs) in front of the LEDs combined with a spatial mask allow for a nearly homogenous beam of 7 mm in diameter at the sample position after being reflected on a dichroic beam splitter (Chroma). The sample illumination, as well as the fluorescence detection, relies on an achromatic doublet (AC300-080-A, Thorlabs) and a meniscus (LE4484, Thorlabs) composing the objective lens set. The implementation of the meniscus reduces the spherical aberration induced by the successive air-glass-BABB planar interfaces [44]. The interaction with the sample takes place in a quartz cuvette (Hellma, HELL704001-30-10) with 3 mm wall thickness filled with BABB acting as an index-matcher. The tip and tilt fine-tuning of the position of the rotation axis has been carried out using aluminum thin sheets following the procedure provided by Watson et al. [45]. The sample embedded in agarose is glued to the lower end of a cylinder magnet facilitating its positioning onto the rotation stage. The sample positioning and projection acquisition process is driven by a custom MATLAB interface for sequential measurement of multiple regions.

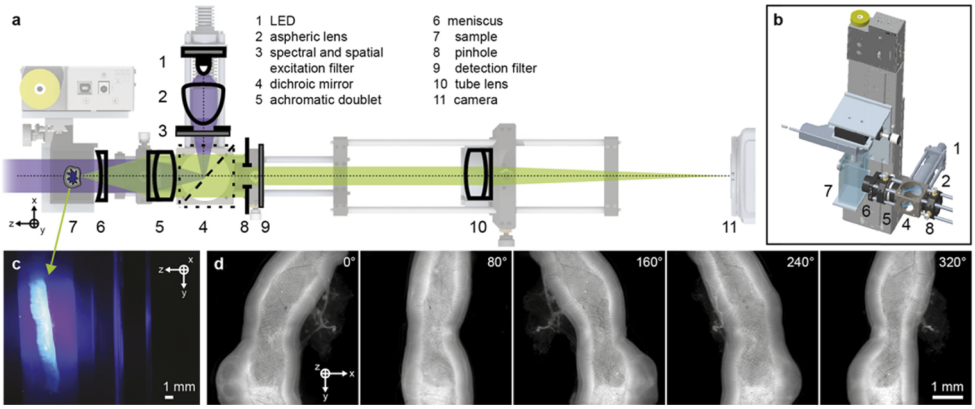

Fig. 1. OPT design. a) Optical layout superimposed with the corresponding mounting system (view from the top). Optical components are numbered from 1 to 11. The optical path of the excitation and detection beams are represented in purple and green, respectively. b) A three-quarter view of the motorized sample positioning stages, as well as the transparent cuvette filled with BABB. c) Photograph taken from the side of the cuvette. A 30 mm long mouse gut sample is embedded into a cylinder of agarose gel submerged in the BABB cuvette. The gel cylinder is glued to the sample holder, which is held together with the rotating motor using a magnet. The gut sample is excited by a LED centered at 415 nm and the fluorescent signal is acquired by the camera for multiple angular positions of the specimen. d) A selection of five projections showing the characteristic acquisitions of cleared samples over 360° in OPT imaging.

Sample fluorescence is transmitted through a dichroic beam splitter, passes through an aperture stop of 2.24 mm diameter and a spectral filter, before being focused onto a sCMOS sensor (ORCA-Flash 4.0, Hamamatsu; pixel size of 6.5 µm) by a tube lens (TTL200-A, Thorlabs). The whole imaging system has a 2.66x magnification and a numerical aperture of 0.03 resulting

Biomedical Optics EXPRESS

in a Huygens PSF [46] that spans from 15 to 20 µm FWHM over the visible range. These characteristics lead to an isotropic voxel size of 2.44 µm. The camera sensor can capture a 5×5 mm^2 FOV, meaning a 5 mm-long specimen region of interest. The images are saved in 16 bit TIFF format and compressed around 8:1 ratio using an efficient lossless compression method [47] to reduce data transfer and storage. The fixed sample is mounted on a stage assembly to perform x and z translation (PT1/M-Z8, Thorlabs), as well as a θ rotation (PRM1/MZ8, Thorlabs). The sample y-axis is scanned vertically using a 300 mm linear translation stage (LTS300/M, Thorlabs) allowing to image specimens up to 10 cm in length in 25 sequential acquisitions (assuming 1 mm overlap). The setup has been designed to allow ease and speed in changing the LED light source, dichroic beam splitter and spectral filters by implementing a custom filter cube slider. Up to five channels are currently available, spanning UV to red wavelengths. Typical measurements are performed with an illumination power density of 0.1 W/cm^2 (at 415 nm) and a camera integration time spanning from 0.01 s to 0.5 s. When imaging with multiple spectral channels, the filter slider is moved manually after the complete acquisition of the sample. Channels are acquired opposite to the excitation wavelength number, from red to UV, in order to reduce photobleaching. The tissue's autofluorescence is excited with a LED centered at 415 nm and spectrally filtered between 400 nm and 440 nm while the emission is measured between 455 nm and 520 nm. Under these conditions, a complete set of 1200 projections spanning 360° can be acquired within 12 minutes. Currently, half of this time is taken by the final positioning step of the rotational stage before projection acquisition and we are currently working on implementing a video acquisition mode to reduce imaging time. Moreover, we plan to adopt a similar scanning approach as reported by A. Arranz et al. [24] in order to reduce the risk of unnecessary photobleaching of the sample when measuring overlapping regions for stitching.

2.3. Image reconstruction algorithm

Our reconstruction process relies on the filtered back-projection (FBP) algorithm [48] for its minimal computational costs. The software is written in Python and calls ASTRA library [49] functions for reconstruction. The full process handles 16-bit data and heavy tasks are all GPU accelerated. Briefly, the measured background signal is first subtracted from all projections. The upper and lower limits of the reconstruction area are defined according to the specimen by applying an intensity threshold value after averaging over all projections. The center of rotation is determined at the 10% top and 10% bottom of the specimen limits by iterating over a guessed interval and maximizing the variance of the reconstruction, as suggested in [50]. After complete FBP reconstruction, a circular mask is applied to the data to remove the out-of-FOV diverging values and the voxels with negative values are set to zero [48]. The 3D image is finally exported as a 3D TIFF file ready for visualization. The full process typically takes less than 5 min with a 3.5 GHz CPU and an enabled 4 Gb GPU (GeForce GTX 750 Ti) acceleration. The script is provided in Dataset 1 [51].

The filtering step in FBP consists in applying a band pass filter to reduce the blurring induced by oversampling the sample near the rotation axis. Such numerical filtering can be applied in the spatial or spectral domain and multiple filter designs have been implemented in the ASTRA toolbox [49]. To select the most appropriate filter type for our application, we rely on the no-reference image quality assessment (NR-IQA) BRISQUE model [52] and the measurement of the spatial resolution determined with fluorescent microspheres. We computed the BRISQUE test on a typical reconstructed gut with a selection of the most common filters used in OPT. As given in Table 1, we obtained better results with the Hamming filter, which confirms our qualitative impression.

The stitching of multiple sub-regions and the registration of multiple spectral channels are realized after volume reconstruction using BigStitcher [53], an ImageJ [54] plugin.

Biomedical Optics EXPRESS

Table 1. No-reference image quality assessment for the most common FBP filters used in OPT

Filter type	BRISQUE score[a]	PSF FWHM[b]
No filter	87.2	No data
Ram-Lak	69.4	31 µm
Shepp-Logan	59.2	34 µm
Cosine	41.3	36 µm
Hamming	38.4	28 µm
Hann	38.8	29 µm

[a]Evaluated after reconstruction of a mouse gut. A lower BRISQUE score means a better-evaluated scene.
[b]Lateral resolution measured using the PSF of reconstructed fluorescent microspheres. The value corresponds to the FWHM of a Gaussian fit realized after intensity integration in the XZ-plane.

3. Results

3.1. Instrument resolution and optimization

To improve the resolution power of a standard OPT scheme, the DOF needs to be adapted to cover at least half of the specimen along the optical axis [6]. This strategy allows for the use of higher NA objective lenses, while acquiring the entire sample over a 360° rotation. The smallest achievable lateral resolution R_{lat} of the optical assembly therefore depends on the radius of the sample r_{sample}. Indeed, the confocal parameter is given by $DOF = 2\pi n{\omega_0}^2/\lambda_0$, where n is the effective refractive index of the medium between the objective lens and the sample, ω_0 the Gaussian beam waist, and λ_0 the vacuum wavelength. By using the relation that converts $1/e^2$ beam waist into R_{lat} FWHM dimension $2\omega_0 = \sqrt{2/\ln 2}\, R_{lat}$, one can derive Eq. (1):

$$R_{\text{lat}} \geq \sqrt{\frac{\ln 2\ \lambda_0\ DOF}{\pi\ n}} = \sqrt{\frac{\ln 2\ \lambda_0\ r_{\text{sample}}}{\pi\ n}} \tag{1}$$

providing the diffraction limit achievable with a standard OPT instrument for a given sample dimension. For our application, given $n = 1.54$, $\lambda_0 = 525$ nm and $r_{\text{sample}} = 2.5$ mm, the smallest achievable R_{lat} is 14 µm.

To optimize the alignment and characterize the resolution of the instrument, we have selected 1 µm fluorescent microspheres as emitting point sources to measure the point spread function (PSF) in the projection space [55] and in the reconstructed volume. These particles are more than five times smaller than the theoretical PSF, thus satisfying the sampling theorem [56], and are sufficiently bright to be imaged by the OPT instrument [57]. Examples of acquired beads are shown in Fig. 2(a) and 2(b), in the projection space and after reconstruction, respectively. According to previously reported works [37,58], we observe that the lateral resolution given by the reconstructed PSFs decreases radially away from the axis of rotation, as shown by Fig. 2(f). Moreover, as detailed by Chen et al. [58] this effect is strongly enhanced when the angular resolution is reduced (see 0.6°, 0.9°, 1.8° and 3.6° data), and 0.3° angular steps (1200 projections) are required to satisfy the minimal number of projections [58] and maintain the PSF optimal over the whole FOV. Similarly, the position of the rotational axis with respect to the focal plane must be finely adjusted in order to remove the *seagull* shape of the PSF shown by Fig. 2(f). This artefact was previously reported by Watson et al. [45] and was attributed by the authors to a refractive index mismatch between the BABB and the agarose matrix or by a too small DOF. Here, we were able to correct the insufficient sampling of the single emitter by optimally positioning the rotation axis with respect to the DOF using five sets of beads acquired with 0.3° angular resolution for

Biomedical Optics EXPRESS

different positions of focus, as shown by Fig. 2(e). After optimization, and by selecting the beads positioned inside a 2 mm radius from the rotational axis, we have measured a mean PSF FWHM of 17 µm in the y-axis and 28 µm in the x- and z-axis (see Fig. 2(c) and 2(d)). The PSF FWHMs are measured after integrating over the corresponding axis. These PSF values demonstrate a sub-28 µm resolution along all 3 dimensions and over more than 60 mm^3 in a single acquisition. As compared to a similar setup dedicated to the mouse brain imaging with a claimed 50 µm isotropic resolution [22], we succeed in improving the resolution by a factor of almost 2. While the y-axis resolution confirms the computed theoretical estimation (15–20 µm) and is slightly superior to the system diffraction limit (14 µm), the x- and z-axis suffer from a resolution loss introduced by the FBP reconstruction. We are currently investigating the implementation of PSF deconvolution [35–37] during FBP to reduce this drawback.

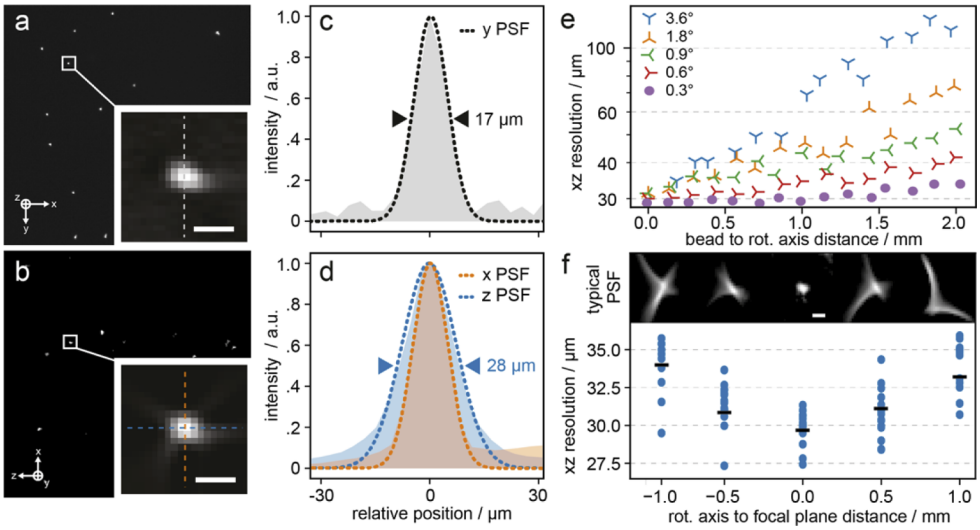

Fig. 2. OPT PSF characterization **a)** Single projection of the acquired fluorescent microspheres. The close-up shows an in-focus microsphere (scale bar = 20 µm). **b)** Y-projection over the reconstructed volume of microspheres to show the XZ-plane PSF. The close-up shows a typical microsphere (scale bar = 20 µm). **c)** Gaussian fit of the PSF integral represented in a) along the Y-axis. The given value is the Gaussian FWHM. **d)** Gaussian fits of the PSF integrals represented in b) along the X- and Z-axis. The given value is the Gaussian largest FWHM. **e)** XZ-plane lateral FWHM of the reconstructed PSF as a function of the distance to the rotation axis for multiple angular resolutions. Each data point is the mean of microspheres included in a 0.1 mm interval. **f)** XZ-plane mean lateral resolution (black line) measured from the reconstructed PSF of fluorescent microspheres as a function of the distance of the rotation axis to the focal plane. 15 PSFs (blue dots) are represented by axis position. A typical PSF for each position is represented at the top of the graph. A seagull shape of the PSF is visible as the distance of the rotation axis to the focal plane increases (scale bar = 20 µm).

3.2. *Mouse gut imaging*

We have imaged a 3-cm long portion of a mouse gut with the use of 2 spectral channels. In addition to the tissue autofluorescence dominated by flavin adenine dinucleotide, we stained the vasculature to emphasize the penetrating vessel network and demonstrate the specificity of our approach. The CD31-mediated vasculature staining is excited at 625 nm and recorded at 690 nm. The full acquisition has been performed by sequentially measuring 8 sub-regions

Biomedical Optics EXPRESS

of 5-mm length and 0.5-mm reciprocal overlap (used for stitching) for each spectral channel. The data acquisition and processing took approximately 190 minutes. The intestinal tissue's macroscopic structure is well preserved after OPT sample processing and details can be observed after volumetric reconstruction. At the centimeter scale, we are able to resolve the mesentery-associated vasculature, which surrounds and supports the gastrointestinal tract (Fig. 3(a)) [59]. In the autofluorescence channel (shown in cyan), individual villi appear as an evenly distributed speckled pattern, as shown in Fig. 3(b). With a cross-sectional view as in Fig. 3(c), we are able to distinguish the submucosa and muscularis layers of the tissue as a distinct ring surrounding the villi structures. When exciting the sample at 625 nm, we observe regions (shown in magenta) with a high density of blood vessels stained by anti-CD31 within the submucosa, where the blood and lymph vasculature networks as well as the enteric nervous system are situated (Fig. 3(c)). This signal is also present in the villi themselves, with an increased concentration of the signal at the ends of the villi closest to the lumen (Fig. 3(c) and 3(d)). This is due to the convergence of the vascular network resident within each individual villus. Thus, OPT can be used as a powerful tool to cross-sectionally image the mouse gut whilst keeping the longitudinal structure intact for subsequent analysis and interpretation in any desired angle and plane (see Visualization 1).

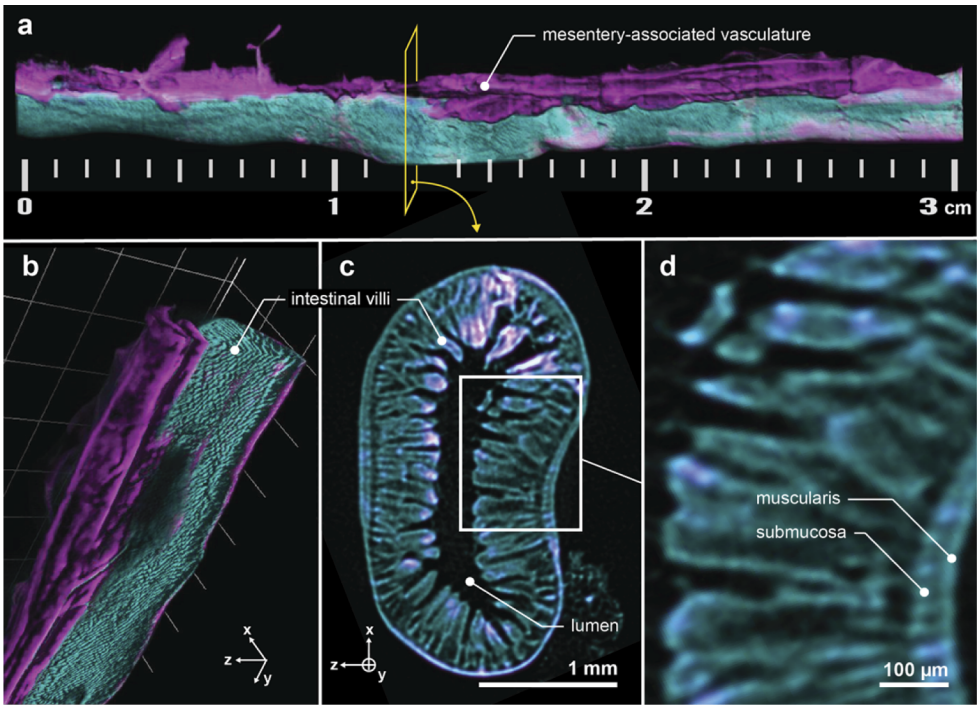

Fig. 3. Mouse small intestine portion imaged by multispectral OPT. For a better 3D experience, see the movie sequence shown in Visualization 1. **a)** 3D blend rendering of a 3-cm long mouse gut portion acquired using 2 spectral channels. The vasculature (magenta) is stained using an anti-CD31 antibody combined with an anti-rat Alexa Fluor 647 secondary antibody and is excited at 625 nm. The tissue is imaged using autofluorescence of flavin adenine dinucleotide excited at 415 nm. **b)** Sliced perspective view of the gut portion emphasizing the intestinal villi structure, as well as the penetrating vessels, and highlighting the 3D advantage of the technique. **c)** OPT cross-section view of the gut showing the submucosa and muscularis layers of the tissue surrounding the villi structures. **d)** Close-up of the typical villi structure with the increased concentration of the vasculature visible close to the lumen as well as in the submucosa and muscularis layers.

Biomedical Optics EXPRESS

4. Conclusion

We described a new multispectral OPT setup optimized for the imaging of the mouse gut and capable of spanning 3 orders of magnitude in size along the 3 dimensions, from a few micrometers to centimeters. We used fluorescent microspheres to optimize the instrument performance and to demonstrate sub-28 μm resolution along the 3 axes.

We showed that the adoption of a multispectral fluorescence approach on cleared samples subject to specific stainings allow to extract anatomic and structural information within a whole organ structure.

Our multispectral OPT setup enables the investigation of the spatial organization of the villi structures, as well as the identification of the vasculature network, of a 3-cm long mouse gut. Besides visualizing the peripheral intestinal vasculature, we observe a high density of blood vessels within the submucosa, as well as clear traces of vasculature at the villi ends closest to the lumen.

We consider this technique a powerful tool for translational gastroenterological research, as it can overcome the typical downsides of conventional techniques, such as limited penetration depth, FOV or resolution. Moreover, it is likely that OPT can be performed with whole-mount stained human specimens obtained from biopsies or surgery, for research and diagnostics in fields like inflammatory bowel disease or cancer immunotherapy. The advantage of OPT as a diagnostic tool is that it is time-efficient, cost-effective and it enables the observation of large volumes with a single acquisition, thus reducing misinterpretations based on poor tissue sampling while using standard histological methods. Moreover, the unique advantage of OPT in enabling bright-field illumination to the mesoscopic range allow 3D imaging from unlabeled samples [28]. Specimen-adapted multispectral OPT imaging has the potential to set the basis for major advances in translational research and patient care, leading to the optimization of current diagnostics.

Funding. Innosuisse - Schweizerische Agentur für Innovationsförderung (31434.1 IP-ICT); Horizon 2020 Framework Programme (686271).

Acknowledgments. The authors are grateful to Theo Lasser for useful discussions and overall support and to François Bugnon and Charles Brack for technical support. AR and AD acknowledge the support from the EPFL Open Science fund.

Disclosures. The authors declare no conflicts of interest.

Data availability. Setup design files, microsphere data and FBP reconstruction code underlying the results presented in this paper are available in Dataset 1 [51]. Data underlying the mouse gut results may be obtained from the authors upon reasonable request.

References

1. V. Ntziachristos, "Going deeper than microscopy: the optical imaging frontier in biology," Nat. Methods **7**(8), 603–614 (2010).
2. A. Fasano, N. P. Visanji, L. W. C. Liu, A. E. Lang, and R. F. Pfeiffer, "Gastrointestinal dysfunction in Parkinson's disease," Lancet. Neurol. **14**(6), 625–639 (2015).
3. T. G. Beach, A.-G. Corbillé, F. Letournel, J. H. Kordower, T. Kremer, D. G. Munoz, A. Intorcia, J. Hentz, C. H. Adler, L. I. Sue, J. Walker, G. Serrano, and P. Derkinderen, "Multicenter Assessment of Immunohistochemical Methods for Pathological Alpha-Synuclein in Sigmoid Colon of Autopsied Parkinson's Disease and Control Subjects," JPD **6**(4), 761–770 (2016).
4. S. A. Schneider, M. Boettner, A. Alexoudi, D. Zorenkov, G. Deuschl, and T. Wedel, "Can we use peripheral tissue biopsies to diagnose Parkinson's disease? A review of the literature," Eur J Neurol **23**(2), 247–261 (2016).
5. A. H. Voie, D. H. Burns, and F. A. Spelman, "Orthogonal-plane fluorescence optical sectioning: Three-dimensional imaging of macroscopic biological specimens," J. Microsc. **170**(3), 229–236 (1993).
6. J. Sharpe, U. Ahlgren, P. Perry, B. Hill, A. Ross, J. Hecksher-Sørensen, R. Baldock, and D. Davidson, "Optical projection tomography as a tool for 3D microscopy and gene expression studies," Science (80-.). (2002).
7. S. Zundler, A. Klingberg, D. Schillinger, S. Fischer, C. Neufert, I. Atreya, M. Gunzer, and M. F. Neurath, "Three-Dimensional Cross-Sectional Light-Sheet Microscopy Imaging of the Inflamed Mouse Gut," Gastroenterology **153**(4), 898–900 (2017).
8. A. M. Cormack, "Representation of a function by its line integrals, with some radiological applications. II," J. Appl. Phys. **35**(10), 2908–2913 (1964).

Biomedical Optics EXPRESS

9. G. N. Hounsfield, "Computerized transverse axial scanning (tomography): I. Description of system," Br. J. Radiol. **46**(552), 1016–1022 (1973).
10. D. W. Holdsworth and M. M. Thornton, "Micro-CT in small animal and specimen imaging," Trends Biotechnol. **20**(8), S34–S39 (2002).
11. A. Kak and M. Slaney, "Principles of Computerized Tomographic Imaging," (1988).
12. A. Liu, W. Xiao, R. Li, L. Liu, and L. Chen, "Comparison of optical projection tomography and light-sheet fluorescence microscopy," J. Microsc. **275**(1), 3–10 (2019).
13. R. J. Bryson-Richardson and P. D. Currie, "Optical projection tomography for spatio-temporal analysis in the zebrafish," in *Methods in Cell Biology* (Elsevier, 2004), Vol. 2004, pp. 37–50.
14. J. McGinty, H. B. Taylor, L. Chen, L. Bugeon, J. R. Lamb, M. J. Dallman, and P. M. W. French, "In vivo fluorescence lifetime optical projection tomography," Biomed. Opt. Express **2**(5), 1340 (2011).
15. J. R. Walls, L. Coultas, J. Rossant, and R. M. Henkelman, "Three-dimensional analysis of vascular development in the mouse embryo," in Current Research in Embryology (2011), Vol. **3**, pp. 222–253.
16. A. Bassi, L. Fieramonti, C. D'Andrea, M. Mione, and G. Valentini, "In vivo label-free three-dimensional imaging of zebrafish vasculature with optical projection tomography," J. Biomed. Opt. **16**(10), 100502 (2011).
17. T. Alanentalo, A. Asayesh, H. Morrison, C. E. Lorén, D. Holmberg, J. Sharpe, and U. Ahlgren, "Tomographic molecular imaging and 3D quantification within adult mouse organs," Nat. Methods **4**(1), 31–33 (2007).
18. M. J. Boot, C. H. Westerberg, J. Sanz-Ezquerro, J. Cotterell, R. Schweitzer, M. Torres, and J. Sharpe, "In vitro whole-organ imaging: 4D quantification of growing mouse limb buds," Nat. Methods **5**(7), 609–612 (2008).
19. V. Kumar, S. Chyou, J. V. Stein, and T. T. Lu, "Optical projection tomography reveals dynamics of HEV growth after immunization with protein plus CFA and features shared with HEVs in acute autoinflammatory lymphadenopathy," Front. Immunol. **3**, 282 (2012).
20. K. Lee, J. Avondo, H. Morrison, L. Blot, M. Stark, J. Sharpe, A. Bangham, and E. Coen, "Visualizing Plant Development and Gene Expression in Three Dimensions Using Optical Projection Tomography," Plant Cell **18**(9), 2145–2156 (2006).
21. T. Alanentalo, C. E. Lorén, A. Larefalk, J. Sharpe, D. Holmberg, and U. Ahlgren, "High-resolution three-dimensional imaging of islet-infiltrate interactions based on optical projection tomography assessments of the intact adult mouse pancreas," J. Biomed. Opt. **13**(5), 054070 (2008).
22. D. Nguyen, P. J. Marchand, A. L. Planchette, J. Nilsson, M. Sison, J. Extermann, A. Lopez, M. Sylwestrzak, J. Sordet-Dessimoz, A. Schmidt-Christensen, D. Holmberg, D. Van De Ville, and T. Lasser, "Optical projection tomography for rapid whole mouse brain imaging," Biomed. Opt. Express **8**(12), 5637 (2017).
23. D. Nguyen, V. Uhlmann, A. L. Planchette, P. J. Marchand, D. Van De Ville, T. Lasser, and A. Radenovic, "Supervised learning to quantify amyloidosis in whole brains of an Alzheimer's disease mouse model acquired with optical projection tomography," Biomed. Opt. Express **10**(6), 3041 (2019).
24. A. Arranz, D. Dong, S. Zhu, M. Rudin, C. Tsatsanis, J. Tian, and J. Ripoll, "Helical optical projection tomography," Opt. Express **21**(22), 25912 (2013).
25. N. Andrews, M. Ramel, S. Kumar, Y. Alexandrov, D. J. Kelly, S. C. Warren, L. Kerry, N. Lockwood, A. Frolov, P. Frankel, L. Bugeon, J. McGinty, M. J. Dallman, and P. M. W. French, "Visualising apoptosis in live zebrafish using fluorescence lifetime imaging with optical projection tomography to map FRET biosensor activity in space and time," J. Biophotonics **9**(4), 414–424 (2016).
26. G. Feng, J. Chen, X. Lu, D. Han, and Y. Zeng, "Laser speckle projection tomography," Opt. Lett. **38**(15), 2654 (2013).
27. Y. Zeng, K. Xiong, X. Lu, G. Feng, D. Han, and J. Wu, "Laser Doppler projection tomography," Opt. Lett. **39**(4), 904 (2014).
28. G. Calisesi, A. Candeo, A. Farina, C. D'Andrea, V. Magni, G. Valentini, A. Pistocchi, A. Costa, and A. Bassi, "Three-dimensional bright-field microscopy with isotropic resolution based on multi-view acquisition and image fusion reconstruction," Sci. Rep. **10**(1), 12771 (2020).
29. J. Mayer, A. Robert-Moreno, J. Sharpe, and J. Swoger, "Attenuation artifacts in light sheet fluorescence microscopy corrected by OPTiSPIM," Light: Sci. Appl. **7**(1), 70 (2018).
30. A. Bassi, B. Schmid, and J. Huisken, "Optical tomography complements light sheet microscopy for in toto imaging of zebrafish development," Dev. **142**(5), 1016–1020 (2015).
31. A. Cheddad, C. Svensson, J. Sharpe, F. Georgsson, and U. Ahlgren, "Image processing assisted algorithms for optical projection tomography," IEEE Trans. Med. Imaging **31**(1), 1–15 (2012).
32. V. Y. Soloviev, G. Zacharakis, G. Spiliopoulos, R. Favicchio, T. Correia, S. R. Arridge, and J. Ripoll, "Tomographic imaging with polarized light," J. Opt. Soc. Am. A **29**(6), 980 (2012).
33. D. Ancora, D. Di Battista, G. Giasafaki, S. E. Psycharakis, E. Liapis, J. Ripoll, and G. Zacharakis, "Optical projection tomography via phase retrieval algorithms," Methods **136**, 81–89 (2018).
34. D. Ancora, D. Di Battista, A. Marcos Vidal, S. Avtzi, G. Zacharakis, and A. Bassi, "Hidden phase-retrieved fluorescence tomography," Opt. Lett. **45**(8), 2191 (2020).
35. A. K. Trull, J. van der Horst, W. J. Palenstijn, L. J. van Vliet, T. van Leeuwen, and J. Kalkman, "Point spread function based image reconstruction in optical projection tomography," Phys. Med. Biol. **62**(19), 7784–7797 (2017).
36. A. K. Trull, J. van der Horst, L. J. van Vliet, and J. Kalkman, "Comparison of image reconstruction techniques for optical projection tomography," Appl. Opt. **57**(8), 1874 (2018).

Biomedical Optics EXPRESS

37. J. van der Horst and J. Kalkman, "Image resolution and deconvolution in optical tomography," Opt. Express **24**(21), 24460 (2016).
38. C. Vinegoni, D. Razansky, J.-L. Figueiredo, M. Nahrendorf, V. Ntziachristos, and R. Weissleder, "Normalized Born ratio for fluorescence optical projection tomography," Opt. Lett. **34**(3), 319 (2009).
39. T. Correia, N. Lockwood, S. Kumar, J. Yin, M.-C. Ramel, N. Andrews, M. Katan, L. Bugeon, M. J. Dallman, J. McGinty, P. Frankel, P. M. W. French, and S. Arridge, "Accelerated Optical projection tomography applied to in vivo imaging of zebrafish," PLoS One **10**(8), e0136213 (2015).
40. L. Chen, Y. Alexandrov, S. Kumar, N. Andrews, M. J. Dallman, P. M. W. French, and J. McGinty, "Mesoscopic in vivo 3-D tracking of sparse cell populations using angular multiplexed optical projection tomography," Biomed. Opt. Express **6**(4), 1253 (2015).
41. L. Quintana and J. Sharpe, "Preparation of mouse embryos for optical projection tomography imaging," Cold Spring Harb. Protoc. 2011, pdb.prot5639-pdb.prot5639 (2011).
42. B. W. Lindsey, A. M. Douek, F. Loosli, and J. Kaslin, "A whole brain staining, embedding, and clearing pipeline for adult zebrafish to visualize cell proliferation and morphology in 3-dimensions," Front. Neurosci. **11**, 750 (2018).
43. R.-A. Lorbeer, M. Heidrich, C. Lorbeer, D. F. R. Ojeda, G. Bicker, H. Meyer, and A. Heisterkamp, "Highly efficient 3D fluorescence microscopy with a scanning laser optical tomograph," Opt. Express **19**(6), 5419 (2011).
44. T. H. Jamieson, "Thick meniscus field correctors," Appl. Opt. **21**(15), 2799 (1982).
45. T. Watson, N. Andrews, S. Davis, L. Bugeon, M. D. Dallman, and J. McGinty, "OPTiM: Optical projection tomography integrated microscope using open-source hardware and software," PLoS One **12**(7), e0180309 (2017).
46. T. Aumeyr, M. G. Billing, L. M. Bobb, B. Bolzon, P. Karataev, T. Lefevre, and S. Mazzoni, "Zemax simulations of transition and diffraction radiation," J. Phys.: Conf. Ser. **517**, 012026 (2014).
47. B. Sanguinetti and C. Clausen, "Method and device for steganographic processing and compression of image data," EP19207833.5 (in Rev. (2020).
48. F. Natterer, *The Mathematics of Computerized Tomography* (Society for Industrial and Applied Mathematics, 2001).
49. W. van Aarle, W. J. Palenstijn, J. Cant, E. Janssens, F. Bleichrodt, A. Dabravolski, J. De Beenhouwer, K. Joost Batenburg, and J. Sijbers, "Fast and flexible X-ray tomography using the ASTRA toolbox," Opt. Express **24**(22), 25129 (2016).
50. D. Dong, S. Zhu, C. Qin, V. Kumar, J. V. Stein, S. Oehler, C. Savakis, J. Tian, and J. Ripoll, "Automated recovery of the center of rotation in optical projection tomography in the presence of scattering," IEEE J. Biomed. Health Inform. **17**(1), 198–204 (2013).
51. C. Schmidt, A. L. Planchette, D. Nguyen, G. Giardina, Y. Neuenschwander, M. Di Franco, A. Mylonas, A. C. Descloux, E. Pomarico, A. Radenovic, and J. Extermann, "Dataset - High resolution Optical Projection Tomography platform for multispectral imaging of the mouse gut," Yareta (2021), https://doi.org/10.26037/yareta:ghbmndkonvd6fmsvqnvyynjnpu.
52. A. Mittal, A. K. Moorthy, and A. C. Bovik, "No-Reference Image Quality Assessment in the Spatial Domain," IEEE Trans. on Image Process. **21**(12), 4695–4708 (2012).
53. D. Hörl, F. Rojas Rusak, F. Preusser, P. Tillberg, N. Randel, R. K. Chhetri, A. Cardona, P. J. Keller, H. Harz, H. Leonhardt, M. Treier, and S. Preibisch, "BigStitcher: reconstructing high-resolution image datasets of cleared and expanded samples," Nat. Methods **16**(9), 870–874 (2019).
54. J. Schindelin, C. T. Rueden, M. C. Hiner, and K. W. Eliceiri, "The ImageJ ecosystem: An open platform for biomedical image analysis," Mol. Reprod. Dev. **82**(7-8), 518–529 (2015).
55. R. W. Cole, T. Jinadasa, and C. M. Brown, "Measuring and interpreting point spread functions to determine confocal microscope resolution and ensure quality control," Nat. Protoc. **6**(12), 1929–1941 (2011).
56. C. E. Shannon, "Communication in the Presence of Noise," Proc. IRE **37**(1), 10–21 (1949).
57. P. C. Goodwin, "Evaluating optical aberrations using fluorescent microspheres: Methods, analysis, and corrective actions," in *Methods in Cell Biology* (Elsevier, 2013), Vol. 114, pp. 369–385.
58. L. Chen, J. McGinty, H. B. Taylor, L. Bugeon, J. R. Lamb, M. J. Dallman, and P. M. W. French, "Incorporation of an experimentally determined MTF for spatial frequency filtering and deconvolution during optical projection tomography reconstruction," Opt. Express **20**(7), 7323 (2012).
59. J. C. Coffey and D. P. O'Leary, "The mesentery: structure, function, and role in disease," Lancet Gastroenterol. Hepatol. **1**(3), 238–247 (2016).